ADVANCED SUSTAINABLE SYSTEMS
www.advsustainsys.com

Sustainable Manufacturing of Graphitic Carbon from Bio-Waste Using Flash Heating for Anode Material of Lithium-Ion Batteries with Optimal Performance

Jasreet Kaur, Amandeep Singh Pannu, Muhammad J. A. Shiddiky, Xiaodong Wang, Paul Frasca, and Jose Alarco**

To address the fundamental challenge of resource sustainability and to effectively deal with issues pertaining to supply chain resilience, cost efficiency, environmental impact, and the ability to meet specific local needs; there is an urgent need for high-grade battery anode materials produced locally from readily available raw materials. In this work, synthesis of high-quality graphitic carbon (GH) derived from human hair is demonstrated using an in-house engineered reactor based on Joule's Flash heating method. The GH is characterized using various techniques to examine its chemical composition, particle morphology, crystallinity, and demonstrate its usability as an anode material for lithium-ion batteries. Fabricated coin cell with active material exhibits a gravimetric capacity of 320 mAh g^{-1} at a current density of 30 mA g^{-1} (equivalent to a C rate of ≈0.1C) over the 100 cycles. The in situ and ex situ studies using XRD, Raman, XPS, and UPS techniques conclude that during the initial charge cycle for GH, lithium ions diffused into the electrode during the resting period are effectively removed. This not only improves the lithium inventory to start with but also mitigates subsequent solvent degradation during solid electrolyte interphase (SEI) formation. Thus, these improvements ultimately enhance the capacity of the anode to 500mAh g^{-1} at a current density of 20 mA g^{-1}. The study offers the potential to initiate a new realm of research by redirecting the focus to a material once considered as mere waste.

1. Introduction

In the current scenario where there is an ever-rising demand for more energy production, the world is witnessing severe pressure on its fossil fuels, viz. coal and petroleum, which are polluting and green-house gas generating as well. For a continuous supply of sustainable and renewable energy and storing this energy in an environment-friendly manner: improving the efficiency of battery devices, for example, lithium-ion batteries is a must. Both natural and synthetic graphite have traditionally been used on the negative terminal as the intercalation anode material for lithium-ion batteries because of its many advantages over other anode materials.[1] The lithium ions are intercalated between the graphene layers that are conjoined sp^2 hybridized hexagonal rings of carbon atoms.[2] These graphene layers making up the graphite structure have π-electron clouds above and below their plane for insertion of incoming Li^+ ions, thus providing a maximum theoretical gravimetric capacity of 372 $mAhg^{-1}$, and volumetric capacity of 719mAh mL^{-1} with the formation of the LiC_6 phase[3] at a low insertion potential of 0.1 V (vs Li/ Li^+).[4] By far graphite is the most stable material resulting in high cycling durability because of low hysteresis[5] accompanying lithium-ion insertion and removal, indicative of reversible lithiation without much capacity loss and volume change.[6] The performance also results from the fact that graphite is a good electrical conductor[7]

J. Kaur, A. S. Pannu, X. Wang, J. Alarco
Centre for Materials Science and School of Chemistry and Physics
Faculty of Science
Queensland University of Technology (QUT)
Brisbane, QLD 4000, Australia
E-mail: apannu@csu.edu.au; jose.alarco@qut.edu.au

DOI: 10.1002/adsu.202300610

J. Kaur, J. Alarco
Centre for Clean Energy and Technology Practices
Queensland University of Technology (QUT)
Brisbane, QLD 4000, Australia

A. S. Pannu, M. J. A. Shiddiky
Rural Health Research Institute (RHRI)
Charles Sturt University
Orange, NSW 2800, Australia

X. Wang
Central Analytical Research Facility
Queensland University of Technology
Brisbane 4000, Australia

P. Frasca
Sustainable Salons Australia Pty Ltd
Sydney, NSW 2000, Australia

and thus the transport of electrons from the anode towards the outer circuit is facile, resulting in high power output. Graphite anodes provide robustness in terms of stable passivating SEI layer formation, involving minimum side reactions[8] and volume changes. This in turn leads to high safety of the battery devices.[9]

The worldwide dependence on electronic devices powered by technological advances and the recent rise in demand for full electric (FEV) and hybrid electric vehicles (HEV) puts further pressure on natural resources, such as petroleum coke and coal tar, which are used to process into synthetic graphite[10] for use in lithium-ion battery anodes. The graphite manufacture and purification processes use a variety of harsh chemicals, such as Hydrofluoric acid (HF), which are extremely deteriorating to the environment.[11] Shifting to alternative sources of carbon and treatment methods, to address sustainability and thus reduce our carbon footprints is imperative. Carbons have been classified as hard and soft with soft carbons defined as the ones easily transforming into graphitic structure at high treatment temperatures while hard carbons do not graphitize.[2] Abundant work has been carried out in this field where precursors such as biowastes and industrial wastes have been used to synthesize carbonaceous materials for use as negative electrodes for lithium-ion batteries. For example, alginate-derived, oxygen-doped hierarchically porous carbons with partially graphitic nanolayers displaying high-rate capabilities were synthesized.[12] Biochar produced from metal-free leather shaving waste after pyrolysis demonstrates a high discharge capacity.[13] Hazelnut shell treated hydrothermally followed by thermal treatment and laser irradiation in liquid has been utilized to generate carbon with beneficial electrochemical properties.[14] Some more biowastes from food and agriculture industry that have been employed to yield carbon materials include banana fibers,[15] wheat stalk,[16] rice husk,[17] corn leaves,[18] etc. The polymeric carbon framework is already available in these raw precursors. Different treatment methods anneal this carbon network into a porous micro or nano crystalline structure with varied degree of graphitization.[12] One eco-friendly carbon-rich source that is abundant and readily available everywhere is human hair.[19] This raw material presents as an incredibly clean source because human hair is made up of fibers of keratin protein[20] that are long chains of amino acids constituted mainly of carbon with some nitrogen and sulfur and very few trace elements. Upon processing, one of the purest forms of carbonaceous material is obtained as nitrogen and sulfur elements escape in their gaseous oxide forms. Applications of hair-derived carbon dots have already been demonstrated in organic and inorganic Light Emitting diodes[21,22] solar cells[23] and sensing.[24]

A plethora of heat treatment methods for anode material preparation have been used in the research literature, from simple tube furnace[25] heating at various temperatures and gaseous environments to using CVD,[26] microwave-assisted synthesis,[27] high-pressure solvothermal reactions,[28] or utilizing the aid of different metallic catalysts.[29] Another processing alternative is the Joule's Flash Heating method, which has been found to be very effective both in terms of time considerations and energy consumption.[30]

We demonstrate synthesis of high-quality (GH) derived from human hair using an in-house engineered reactor based on the Joule's Flash heating method; characterize it using various techniques to examine its chemical composition, particle morphology, crystallinity, and composition; and demonstrate it application as anode material for lithium-ion batteries. The uniqueness of this method is that while biowaste-based carbonaceous materials are mostly non-graphitic (soft or hard carbons) and suffer from drawbacks such as high irreversible first cycle capacity loss, slanting voltage profiles, and higher voltage hysteresis during cycling; our human hair biowaste precursor converts into GH structure. This said, manufacture of GH otherwise depends mainly on fossil fuel precursors unlike the biowaste precursor employed here.

2. Experimental Methods and Procedures

2.1. Material Synthesis

The raw material of mixed human hair (HH) was collected from the hair-dressing industry, particularly from Sustainable Salons. The material was washed with isopropyl alcohol (IPA) and rinsed with water and dried at 70 °C. The dried hair was chopped and ground to yield a fine powder. This powder was compressed to form small pellets suitable for loading between the carbon electrode and the porous copper electrode within a quartz tube of 15 mm diameter where the flash reaction would occur. **Figure 1** shows the small pilot demonstration devices.

In the flash reactor,[31] the flash was generated with the help of an aluminium electrolytic capacitor bank, with each capacitor of 400 V, 18 mF. The compressed pellet reduced the sample resistance to the flash. The capacitors were charged with a light-emitting diode (LED) power supply in parallel and later put into series using a series-parallel switch. A bleed resistance (variable resistor) was used across the capacitors to discharge them completely after the reaction. A kill safety switch was implemented to switch off the reaction at any time and discharge the capacitor across the bleed resistance. A 20mH, 20 A inductor was used to protect the relay as well as the whole assembly from high current during switch on/off operation. Further, to protect the inductor from the surge of voltage during the switching operation, a diode (1200 V, 560A) was placed in parallel with the inductor. The capacitor was discharged across the samples at 400 V with a discharge time of 150 ms. The number of pulses was optimized to achieve >70% graphitization for the given sample. The as prepared sample of graphite from human hair was labeled GH. The XRD material analysis indicates 96 percent graphitization of sample.

2.2. Material Characterization

As already mentioned, the raw precursor is a sample of powdered human hair (HH). Wavelength Dispersive–XRF analysis was performed on the precursor in a Bruker S8 Tiger Series II Wavelength Dispersive X-ray Fluorescence (WD-XRF) Spectrometer before and after flash heat treatment to determine chemical compositions of the precursor as well as of the processed anode material. To find out the amount of carbon, nitrogen, hydrogen, and sulfur in the raw material, a Thermoscientific FlashSmart CHNS/O analyzer was employed. For this analysis, the raw sample was combusted to 1000 °°C upon the addition of vanadium

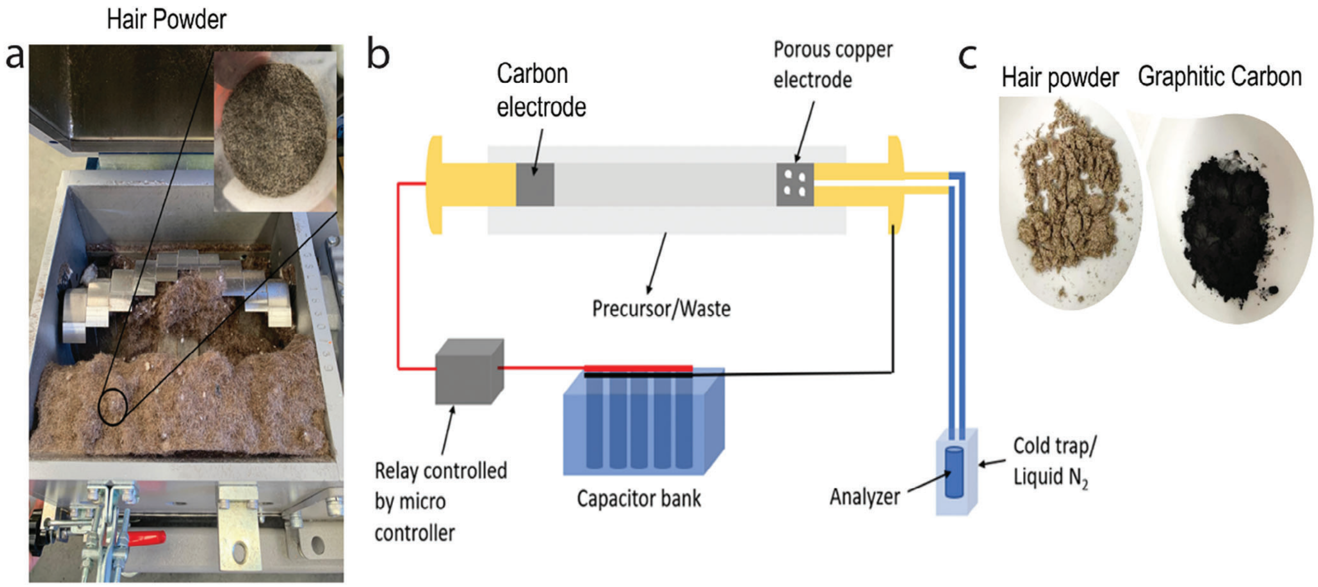

Figure 1. Hair powder production at small pilot demonstration scale: a) photo of the hair grinding device; b) schematic of the flash reactor for generating high temperature for short intervals of time; c) Hair powder and graphitic carbon.

pentoxide. Similarly, the amount of carbon, nitrogen, and sulfur in the processed bulk anode material after precursor treatment was also found using a Leco 23 084 CNS analyzer. The oxygen and hydrogen content were determined with the FlashSmart CHNS/O

To help understand the pattern and impact of the high-temperature treatment on the precursor, a thermogravimetric analysis was performed on a Netzsch Jupiter 449F3 high-temperature Simultaneous Thermal Analyzer. To have an insight into how the heat capacity of the active material (GH) changes with temperature, the change in heat flow as a function of temperature was measured using differential scanning calorimetry. Measurements were also conducted to determine the pore size and surface area of the material. Before adsorption, the sample material was degassed under vacuum on a Micromeritics Smart Vac Prep Sample Degas System. As the sample was very stable, it was degassed at 300 ^{0} C and a vacuum pressure of the order of 150 milli torr for 24 h. After cooling down the sample, it was transferred to Micromeritics Tristar II 3020 Surface Area and Porosity Analyzer for surface area and porosity measurement using nitrogen gas at 77K for adsorption and desorption.

To measure the degree of crystallinity of the sample and phase identification after treatment, powder X-ray diffraction patterns were acquired on a Rigaku Smart Lab X Ray Diffractometer using copper Kα radiation and a CBO-α mirror[32] in Bragg-Brentano geometry. To investigate the surface morphology of synthesized materials, scanning electron micrographs were recorded on a JEOL7001F SEM. An EDS detector was used with this instrument to create EDS maps. To investigate nanostructures of the materials and particle size distributions, high-resolution transmission electron microscopy (HRTEM) images of samples were obtained with a JEOL 2100 TEM, operated at an accelerating voltage of 200 KV. To collect chemical information such as functional groups and bonds present in the synthesized material, FTIR spectra were obtained using a Nicolet iS50 FT-IR instrument with in-built diamond attenuated total reflectance (ATR) and further Germanium ATR. The spectra were also measured using the DRIFTS mode to verify the possibility of even the slightest different functional groups on the surface if present.

To quantify elements and their chemical state on the surface of materials, X-ray Photoelectron Spectroscopy (XPS) was performed on an Axis Supra (Kratos) instrument with aluminum Al Kα ($h\nu = 1486.7$ eV) radiation. The powdered sample was fixed on a glass slide with the help of carbon tape and plasma was cleaned before mounting. The sample was grounded with carbon tape to prevent charging during the experiment. To investigate the electronic work function and ionization potential of the fabricated electrodes, Ultraviolet photoelectron spectroscopy (UPS) studies were performed on the Axis Supra (Kratos). To further investigate the chemical structure, phase, and crystallinity of the surface of the material, Raman spectra of the powdered sample was collected on a Renishaw Qontor microscope equipped with a long working distance 50× objective lens and a 532 nm Ar+ laser light source.

2.3. Electrochemical Characterization

The slurry for anode coating was prepared in the ratio of 90:5:5 for active material: conductive carbon (super P): binder (Polyvinylidene fluoride PVDF). Fifty milligrams of PVDF was uniformly mixed with 2 g of N-methyl-2- pyrrolidone (NMP) solvent using a whirl mixer. Nine hundred milligrams of active material and 50 mg of Super P were added, after grinding them together using a mortar and pestle to the uniform binder/solvent mixture and were mixed further for 30 min. The anode slurry was coated on copper foil with a wet thickness of 120 micrometers using the Doctor Blade method. The coated foil was dried in a vacuum oven at 120 °C overnight and punched into discs of 2 cm^2. CR2032 coin cells were assembled for half-cell testing in an Argon-filled glove box with O_2 and moisture content below 0.1 ppm. Lithium foil discs were used as negative electrode with Celgard membrane of thickness 25 micrometers as separators, GH-coated copper foils as positive working electrodes (or as cathodes when Li foils act as anodes) and 1 M $LiPF_6$ dissolved in ethylene carbonate, dimethyl carbonate and diethyl carbonate solution (1.0 M $LiPF_6$ in EC/DMC/DEC = 1:1:1, v/v/v) as electrolyte. The thickness attributed to spacer discs was 1 millimeter. The Galvanostatic charge and discharge (GCD) cycle test and rate test were performed in a voltage window range of 0.01 and 1.5 volts on a Neware BTS4000 potentiostat. Cyclic Voltammetry (CV) runs on electrodes were carried out using a BioLogic, VMP-300 system between 0 and 1.5 V at a scan rate of 0.5 mV per second.

The slurry prepared by the above method was also coated onto a copper mesh current collector and used as working electrode in an EL-CELL ECC-Opto-Std test cell with lithium foil as counter electrode for in situ XRD measurement for the initial two lithiation and de-lithiation cycles. The electrolyte was filled in the test cell using negative pressure and the cell was operated in a two-electrode combination system. A beryllium window was used in the test cell to perform XRD measurement in reflection mode. The in situ XRD measurement was conducted in the Rigaku SmartLab X-ray Diffractometer, using a variable divergence slit of 5 mm X-ray footprint on the Be window and fixed knife edge above the Be window to block air-scattering background. The in situ XRD patterns were collected every 13 min and half-cell galvanostatic charge–discharge was carried out at C rate of 0.05C using a Gamry Instruments single channel potentiostat. Ex situ experiments were also performed using Raman and XPS studies. UPS studies for calculation of work function on these electrodes were further undertaken as part of ex situ studies. Electrode discs at various stages of cycling from the EL-CELL test cell, namely, pristine (freshly casted and dried), at rest (state of conditioning), discharged state, and charged state, and one disc that was initially charged were retrieved and studied. For obtaining the ex situ Raman spectrum, the electrodes were taken out of the EL test cell inside an argon filled glove box, washed with dimethyl carbonate solvent, and dried before mounting in the dried test cell again to maintain an air-free environment for Raman studies. The discs were also mounted on a stub inside the glove box and transported to the Kratos instrument with the aid of an air-free sample transfer holder. A side-end entry stub bar was used to affix the mounted stub for XPS studies.

3. Results and Discussion

Results from a combination of techniques are shown and discussed below, providing a thorough characterization of the microstructure and properties of the materials.

3.1. Material Characterization

3.1.1. Chemical Composition

The WD XRF helps to determine the inorganic composition of elements present in the human hair (HH) raw precursor powder, as well as in the (GH) resulting from the flash treatment. Similarly, the amount of hydrogen, sulfur, and other 2nd period elements such as C, N, and O in bulk samples were also determined using an elemental analyzer. **Table 1** gives the percentage composition of each element.

A thermogravimetric analysis experiment was performed on the HH sample which was heated up to 1500 °C in an argon atmosphere. The initial loss in mass is due to the removal of moisture and any adsorbed oxygen on the surface of the sample when heated up to 200 °C. The onset of carbonization occurs at 260 °C and peaks at 313 °C when there is a maximum reduction in mass at a rate of 4.55 percent per minute as shown by the differential thermal analysis curve in **Figure 2**a. The differential scanning calorimetry curve in Figure 2b suggests that the transformation of BMHH to GH is an exothermic reaction. A large amount of heat flow takes place between 900 and 1300 °C. A look at the DTG curve suggests almost no change in mass between these temperatures. This heat change is therefore associated with latent heat for the phase change of the carbonized material, implying graphitization in action at this temperature.

FTIR spectra could not be obtained on a diamond and then on the germanium crystal using the ATR mode on Nicolet iS50 FT-IR because of the high absorbance of the carbon material. To obtain a quality spectrum, DRIFTS mode was employed and powdered samples were used. GH was transparent to any peaks suggesting no functionalities or oxygen present in the sample. For more details refer to Supporting Information.

3.1.2. Pore Structure

According to the IUPAC recommendation, the physisorption isotherm in Figure 2c is a composite Type II-IV P-V graph at a constant temperature, where the adsorption loop is type II. The average pore size varies between 2 to 16 nm, thus the nano porous material is actually mesoporous which displays a type IV curve.[33] Adsorption occurs in three steps here. Monolayer adsorption is followed by multilayer adsorption on the mesopore walls. It is visible that adsorption and desorption curves do not coincide resulting in a hysteresis of the type H3 seen in this graph.[34] This arises due to the third and final step of capillary or pore condensation where nitrogen gas condenses to a liquid-like phase inside the pores. The hysteresis loop of this type (see **Figure 3**c) suggests the presence of non-rigid aggregates of plate-like particles that are non-uniform in size. The BET surface area of material which includes the external surface as well as the interconnected, open pore area is 13.2386 ± 0.0384 $m^2\ g^{-1}$. From the BJH adsorption pore distribution report that is the most suitable method for mesopore size analysis, it is found that the total pore volume is 0.018 $cm^3\ g^{-1}$ and that there are no pores that are simultaneously open at both ends. The pore size calculated by the BJH method from the adsorption branch of the loop shows pores ranging between 2.5 and 4 nm in diameter making up for most of the pore volume as visible in Figure 2d. The total pore area is 13.107 $m^2\ g^{-1}$. The electrochemical properties arising from the transfer of lithium ions in and out of material pores could be attributed to the large BET surface area accompanied by high number of pores with small pore width making up most of the pore volume.

3.1.3. Particle Morphology, Crystallinity, and Phase Composition

To investigate the particle morphology and crystallinity of the materials, scanning electron microscopy (SEM), transmission elec-

Table 1. Quantitative elemental analysis before and after the treatment method of the precursor material and processed anode material determined using WDXRF and CHNS/O analyzer.

Composition		Raw Precursor		Processed material
Inorganic composition (percentage)	Cl 0.0452	Cu 0.006	Mg 0.050	Cl 0.0127
	Ca 0.218	Sr 0.001	K 0.015	Ca 0.072
	Ti 0.002	Al 0.009	Mo 0.001	Ti 0.008
		Zn 0.015		Cu 0.004
Organic composition (percentage)		C 43.73		C 100
		N 13.32		N 0.066
		S 3.48		O 0.26
		H 6.69		S, H nil

tron microscopy (TEM), and high-resolution transmission electron microscopy (HRTEM) images of samples were obtained with a JEOL 7001F SEM and a JEOL 2100 TEM, operated at accelerating voltages of 20 and 200 KV, respectively.

The High-resolution TEM images confirm the presence of highly crystalline material with layered structure. Analysis of Figure 3a reveals stacking and folding of ribbon-like plates demonstrating layered structure of graphite. Additionally, high-resolution TEM (HRTEM) images in Figure 3b demonstrate the crystalline nature of the sample with an average fringe distance of 3.48 A^0 Å (refer to Figure S2, Supporting Information). The particle size, topography, and surface morphology of the sample was investigated with SEM. The images were taken at an accelerating voltage of 10 KV with a probe current set at 8. Figure 3c indicates uniform particle size distribution within 5–10 µm. The flake structure from the graphitized sample is visible with interstacked layers when a higher resolution scan was recorded, as shown in Figure 3d. To analyze the chemical composition, EDS spectroscopy mapping was performed on this particle (Figure 3e). The EDS spectrum (Figure 3f) indicates pure GH. However, some of the particles (Figure 3g) show adsorbed surface oxygen apart from GH in the EDS mapping (Figure 3h,i).

To further investigate the structure of synthesized GH and measure the disorder, Raman spectrum of the GH sample was

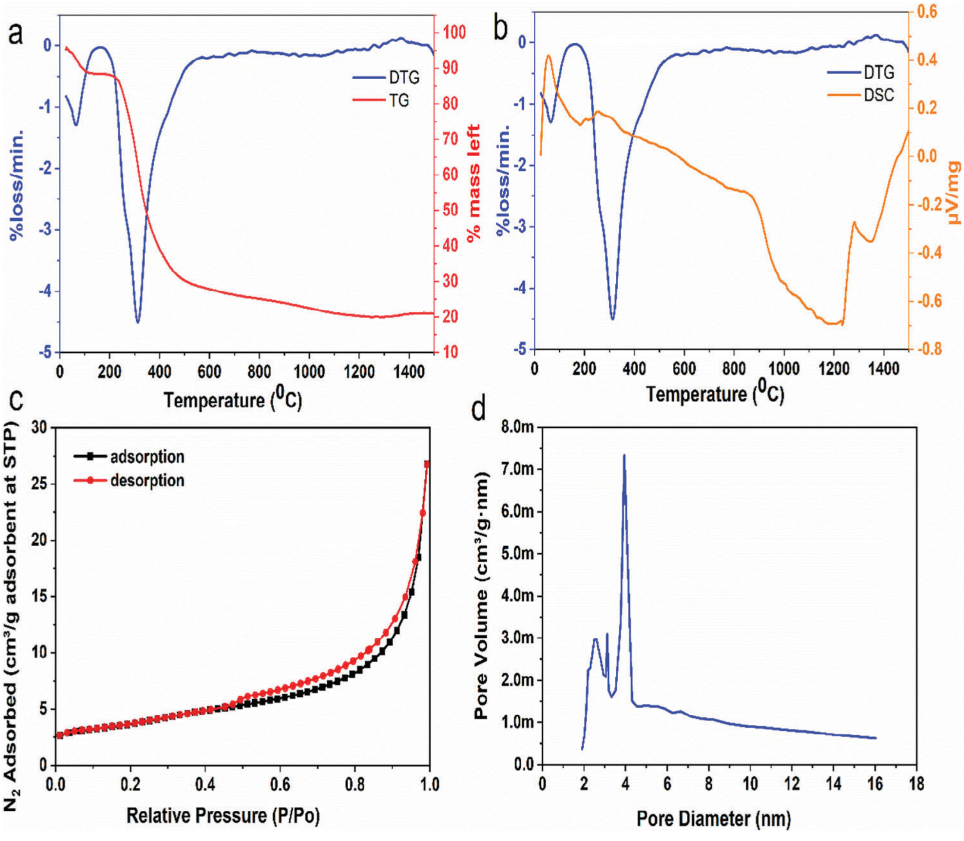

Figure 2. a) mass loss of precursor as a function of temperature and corresponding DTG curve b) change in heat flow to precursor as a function of time and same DTG curve c) Nitrogen adsorption–desorption isotherms d) BJH pore size distribution.

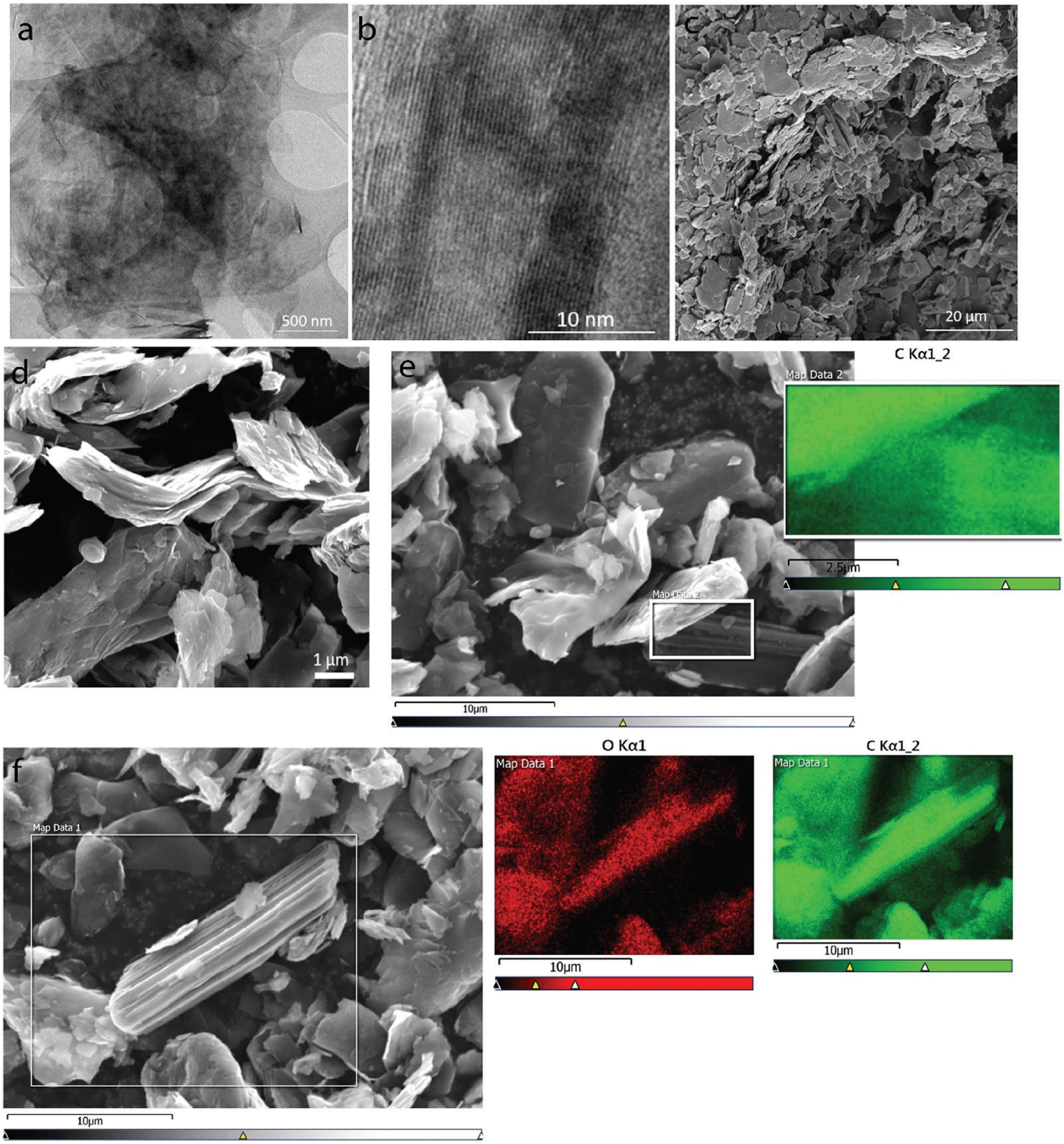

Figure 3. a) The Transmission electron microscope (TEM) image of (GH). b) High-resolution HR-TEM of GH showing fringes of the sample. c) Scanning electron microscope (SEM) image with in-beam secondary detector. d) SEM image at higher resolution. e) Area for mapping Energy dispersive spectrometry (EDS) of sample in SEM. f) Mapping indicates only carbon presence. g) Electron map area for EDS h) Map data 1 showing the presence of Carbon and i) map data 2 showing the presence of adsorbed oxygen.

recorded (**Figure 4a**). The peak at 1582cm^{-1} corresponds to the G band arising due to the E_{2g} optical mode, confirming the presence of graphitic sp^2 structure.[35,36] The occurrence of a peak at 1348 cm^{-1} (D band) depicts synthetic graphite with defects. The peak at 2715cm^{-1} is the 2D band arising due to the overtone of the D band. The intensity ratio (I_D/I_G) for the D and G bands is used for understanding the defect quantity in graphitic materials as well as the stacking order.[37] The I_D/I_G ratio has been calculated to be ≈0.2 and thus, the low ratio signifies high degree of sp^2 bonded ordered structure or graphitisation in the sample. Further, the XRD pattern of the GH sample (Figure 4b) fits well with the reference pattern (ICDD PDF 04-007-8496[38]) for the

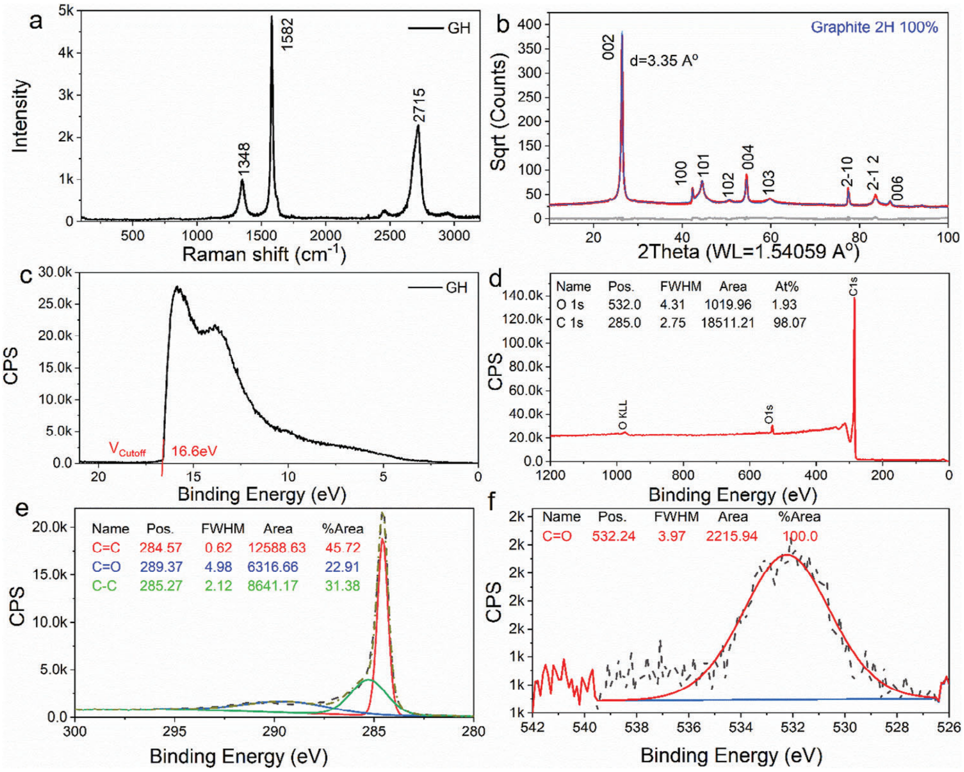

Figure 4. a) Raman spectrum of GH. b) Rietveld refinement of the XRD pattern of GH powder, $R_{wp} = 8.314\%$. c) Ultraviolet photoelectron spectroscopy (UPS) of GH. d) XPS survey spectra of GH powder. e) High-resolution C1s XPS spectra of GH and f) O1s spectra of GH.

graphite-2H crystal structure. The refined lattice parameters are a = 2.4582(1)Å and c = 6.7147(6)Å, which corresponds to d_{002} = 3.3574 Å. The degree of graphitization[39] calculated from this value for this GH product s approximately 96.1%. Figure 4b has a slight deviation between calculated XRD pattern and measured data because of anisotropic peak broadening measured from the sample (e.g., 101 peak is much broader than 100 peak), most likely due to turbostratic disorder commonly seen in graphite structure. It is reported in the literature that the introduction of oxygen into the structure would make an extra graphitic peak to appear at 10.3 ° 2θ and a broad peak to appear ≈23.5° 2θ.[40] The apparent absence of these two XRD features in Figure 4b suggests the adsorbed nature of oxygen was only onto the surface of graphite. The work function of GH can give potential insight into the application of this material as an electrode material in Li-ion batteries. To investigate the work function of GH, the UPS of the sample was recorded (Figure 4c). The V cutoff of GH was measured to be 16.6 eV, resulting in 4.62 eV as the work function for GH. To further calculate the amount of oxygen adsorbed on the surface of the sample XPS studies were done. The XPS survey spectrum of the sample (Figure 4d) shows carbon to be 98.07% (C1s, 285 eV) while adsorbed oxygen is ≈1.93% (O1s, 532 eV). To further investigate the nature of carbon bonds, high-resolution carbon (C1s) scan was recorded. The high-resolution C1s spectrum of GH (Figure 4e) can be deconvoluted into three peaks: the strongest peak at 284.57 eV is attributed to C═C double bond (48.37%), the second peak at 285.27 eV is ascribed to C─C bond (29.67%) and the third (weakest) peak at 289.20 eV corresponds to C═O bond (21.96%). The small amount of covalently bonded surface oxygen with carbon is also confirmed in a high-resolution oxygen scan (O1s) with a single peak at 532.16 eV (Figure 4f).

3.2. Electrochemical Results

The assembled half cells with GH as anode and lithium foil as reference electrode had a mass loading between 4.5 and 6.3 milligrams of total material on the copper current collector. These were cycled at a current density of 50 mA g^{-1} of active material initially for 3 cycles of discharge and charge to ensure a steady formation of the solid electrolyte interface (SEI) layer. The discharge (lithiation of graphite) and charge (delithiation of graphite) steps were run at constant current constant voltage (CCCV) mode. The detailed lithiation of the GH anode involves discharge at a constant current until the voltage drops to 0.01 V and then holds the coin cell at that voltage until the current tapers to 5 percent of the original current. Similarly, delithiation of GH anode was made certain by charging the coin cell to 1.5 V while supplying a constant current and then holding it at the constant voltage until the current falls to 5 percent of the original value. The discharge and charge capacities of this coin cell are related to the amount of charge that can be stored and released, respectively via lithium ions at the working electrode. The first cycle discharge and charge values were 470 and 340 mAhg^{-1}. However, it is worth mentioning that it took only 14 and 7 h respectively, for the first discharge and first charge of the coin cell. The two consecutive cycles happened at C/9 discharge rate and C/7 charge rate. The subsequent 5 cycles were then run at current density approximately three

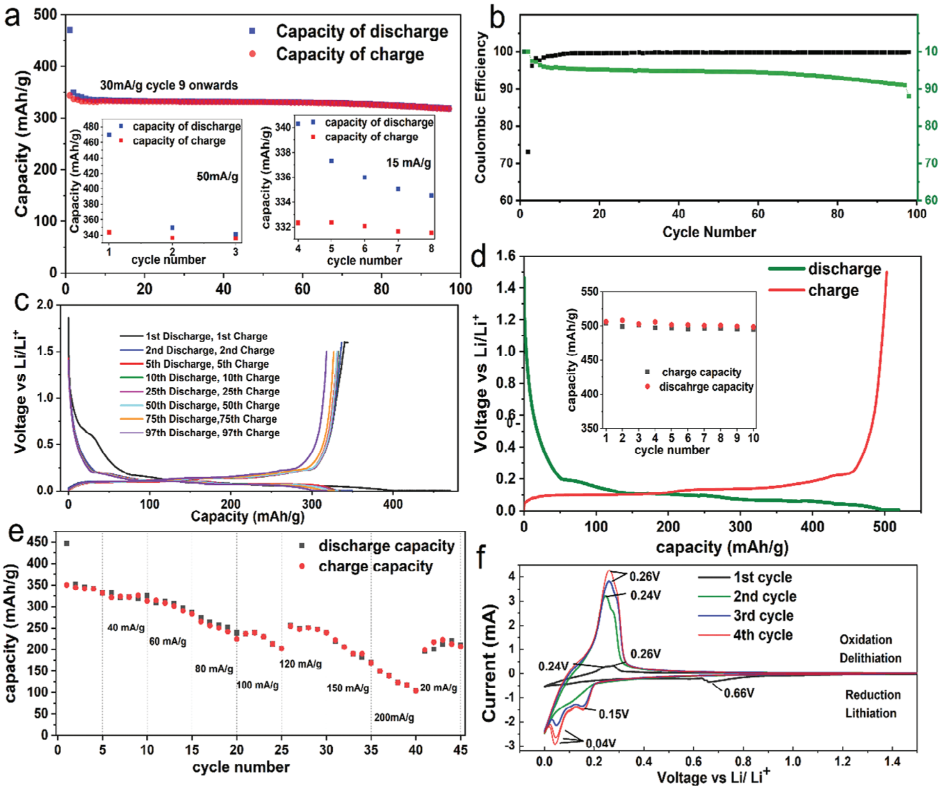

Figure 5. Electrochemical performance of GH: a) cycle performance b) coulombic efficiency and capacity retention c) GCD curves d) GCD curve if half-cell is charged prior to first discharge. The inset displays numerical discharge and charge capacities for the first 10 cycles e) rata capability test (f) CV curves.

times lower, that is, 15 mA g^{-1} in order to tune to a C rate of 0.05C (or C/20) while the actual discharge and charge happened at C/24 and C/22, respectively. Similarly, the next 90 cycles were obtained at a current density of 30 mA g^{-1} that corresponds to a C rate of 0.1C whereas the obtained C rates were C/12 and C/11 respectively for the discharge and the charge step. The cycle performance is shown in **Figure** 5a. while the GCD curves from the cycling are depicted in Figure 5c.

Typically, the pristine lithium-ion cell assembled in complete, full-cell mode is present in a "graphite" discharged (delithiated) state, and hence every single cycle involves a charge step followed by discharge. Initially, the amount of lithium transferred to the anode during the charge step is more than the amount of lithium which is extracted from the anode during the discharge step, as certain amount of lithium fixes itself as part of the SEI film formation via irreversible reactions involving the electrolyte and other side reactions occurring. Therefore, the Columbic Efficiency (CE) of the lithium-ion battery, which measures the efficiency of charge transfer via lithium shuttling, can be defined as the ratio of total charge transfer involved during the discharge step (delithiation of the anode) to the total charge transfer during the charge step (lithiation of the anode) of the same cycle and it will always be <1, though the percentage approaches close to 100 percent, a typical observation for lithium-ion batteries. As an example, CEs of Li || NMC811 coin cells in two different electrolytes are quoted to be 99.69% (cycled stably for >180 cycles) and 99.76% (cycled for 50 cycles).[41]

The situation is somewhat different when the cell is cycled after its assembly in half cell mode to test the anode performance. Here the full-cell anode becomes the half-cell cathode while the lithium foil acts as the anode, if we consider the voltage polarity used at the respective electrodes. The cell is assembled in charged state with an open circuit voltage equal to the difference in potential between both electrodes to produce electrical energy. In such a cell, the initial discharge step involves lithiation of the working electrode (now cathode), followed by a charge step involving delithiation. The SEI layer formation will occur on the working electrode with the discharge of the half-cell and hence the capacity of charge will be less than the capacity of discharge. Thus, the CE of such a cell could be better defined as the ratio of capacity of charge to the ratio of capacity of discharge of the same cycle.

The coulombic efficiency improves from 96 percent for the 2nd cycle to 99 percent nearing 100 cycles, displaying highly efficient charge transfer from lithium ions by the GH anode material. (Figure 5b) The Capacity Retention which is the ratio of discharge capacity of a given cycle to the initial discharge capacity provides important information on the cycling stability and life of the anode. The coin cell retains 88 percent of the capacity from the 2nd cycle (1st cycle not accounted as it involves irreversible SEI formation) after ≈100 cycles. (Figure 5b) The observation is consistent with very little capacity fading. Typical cyclic voltammetry curves (Figure 5f) were obtained at a scan rate of 0.05 mV per second. In the first cycle, during the cathodic sweep, an irreversible SEI formation peak is observed at 0.66 V. Reversible

Table 2. Capacities of graphitic anode references at similar current densities.

Anode material	Current rate (in terms of C Rate or Current Density)	Capacity in mAhg^{-1}
Meso-carbon microbead (MCMB) carbon graphite (Nippon Carbon Co. Ltd)[42]	C/12	337 after 100 cycles
	C/2	≈70 after 5 cycles
Natural vein graphite from Sri Lanka (needle platy variety)[43]	C/5	378 after 50 cycles
	C/2	315 after 5 cycles
Shot coke precursor treated at 2800 °C	30 mA g^{-1}	396.4 first discharge and 313.7 first charge capacity
Artificial graphite scraps graphitized at 3000 °C[44]	15 mA g^{-1}	337after 3rd cycle
Bituminous coal precursor treated at 2800 °C[45]	C/10	≈320 after 10 cycles
	C/5	≈275 after 20 cycles
	C/2	≈235 after 30 cycles
Graphitic Carbon from human hair in this study	15 mA g^{-1} equivalent to C/24 Discharge and C/22 Charge	335 after 8 cycles
	30 mA g^{-1} equivalent to C/12 Discharge and C/11 Charge	320 after 100 cycles
	50 mA g^{-1} equivalent to C/9 Discharge and C/7 Charge	340 after 3 cycles
	200 mA g^{-1} equivalent to C/2 Discharge and 1C Charge	166–100 in 5 cycles from 36th to 40th cycle

lithiation is observed at 0.15 and 0.04 V in all 4 cycles. During the anodic sweep, similar reversible delithiation peaks, symmetric to the ones below, are observed at 0.24 and 0.26 V. The rate capability tests were performed on the GH electrode (Figure 5e). A drop in open circuit voltage from the one measured inside the glove box after fresh assembly to that measured after an overnight rest period was observed in almost every coin cell. This sighting led to exploring the effect of an initial charge step before the original discharge of the coin cell and a consistent, reproducible charge capacity of 500 mAhg^{-1} was obtained for >10 cycles at a current density of 20mAg^{-1}, as depicted from GCD curves in Figure S3 (Supporting Information) which shows 1st, 5th, and 11th charge–discharge curves. Figure 5d demonstrates the first charge and discharge curve from the same graph. The inset in the same graph displays numerical discharge and charge capacities for the first 10 cycles.

The **Table 2** demonstrates capacities of few other graphitic anode references at similar current rates. As mentioned earlier the current density of 30 mA g^{-1} was provided to tune a C rate of 0.1 C, while the actual discharge and charge rate remained C/12 and C/11, respectively, over the 100 cycles. The highest current density of 200 mA g^{-1} supplied during rate capability testing translated to a C rate of 0.5 C while discharging and 1 C while charging.

3.3. In Situ and Ex Situ Studies

The ex situ and in situ electrochemical studies present interesting insights bolstering the observed electrochemical properties of the material. It was observed that the discharge capacity of the GH material is higher when the first step in cycling is a small charge of the half-cell which is followed by a discharge, as opposed to starting with an initial discharge. To investigate this further, ex situ studies were carried out.

3.3.1. Ex Situ XPS Studies

Ex situ XPS studies were carried out on solvent washed electrode discs at various stages of cell cycling after transferring them to the instrument using an air-free transfer holder. Sample discs were sputter cleaned and depth profiled with the argon gas cluster ion source. For comparison and correlation, the pristine electrode survey spectrum (wide scan, **Figure 6a**) was also recorded. The wide scan indicates the presence of active carbon material (87.68%), fluorine (F1s, 4.83%) from PVDF binder, and adsorbed oxygen (O1s, 7.49%). The lithium starts to diffuse as soon as the half-cell is assembled as indicated by the survey spectrum of the electrode at rest (Figure 6b) showing the presence of lithium (Li 1s, 21.77%) (that is absent in the fresh material). Apart from oxygen (O1s, 8.31%), carbon (C1s, 25.80%), and phosphorus (P 2p, 2.27%), there is a signal for silicon (Si 2p, 3.08%) which can be attributed to impurity. Since initially diffused lithium is seen at the rest state, the cell was charged to remove the diffused lithium during the rest period. After charging, the survey spectrum of the anode was recorded again. The wide scan (Figure 6c) shows no lithium presence. However, copper (Cu 2p, 1.86%), which is due to a small, exposed part of the anode is seen in addition to oxygen (O 1s, 10.13%), carbon (1s, 53.26%), fluorine (F 1s, 30.33%), phosphorous (P 2p, 2.22%) and silicon impurity (Si 2p, 2.20%).

As expected during the discharging, the lithiation of the anode will take place, hence the wide scan of the discharged electrode (Figure 6d) shows a higher content of lithium (Li 1s, 29.68%) relative to other scans, apart from other elements. It becomes clear from the above investigation that during the rest state, the lithium ions have physically diffused to the anode and, therefore, initially charging the coin cell puts all the lithium back to start with and thus delivers higher capacity compared to the coin cell which is discharged first. This observation was also evident from electrochemical charge–discharge galvanostatic studies while comparing GCD curves from Figure 5c,f.

3.3.2. Ex Situ Raman Studies

To further investigate the effect of first charging the half-cell rather than discharging on the phase composition at the surface of the anode, ex situ Raman was also performed. The same electrodes used for ex situ XPS studies were mounted in the test cell under a transparent glass slide to measure the Raman

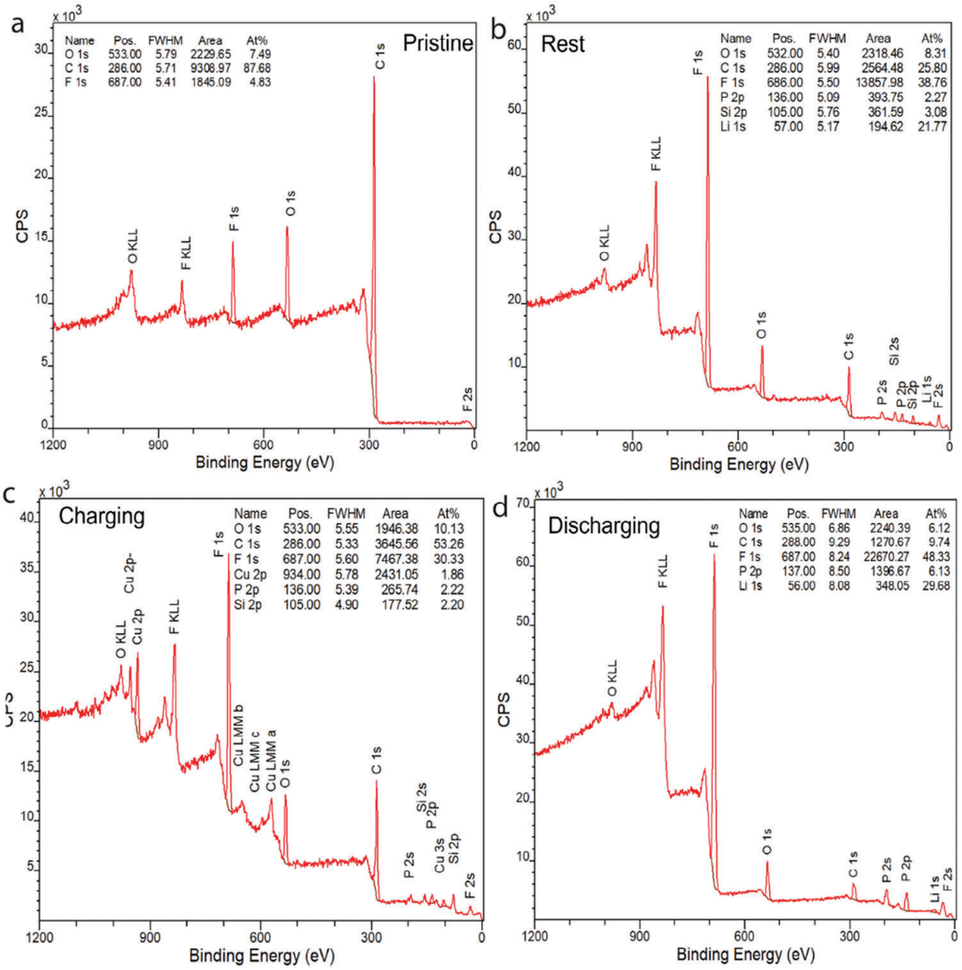

a

Name	Pos.	FWHM	Area	At%
O 1s	533.00	5.79	2229.65	7.49
C 1s	286.00	5.71	9308.97	87.68
F 1s	687.00	5.41	1845.09	4.83

b

Name	Pos.	FWHM	Area	At%
O 1s	532.00	5.40	2318.46	8.31
C 1s	286.00	5.99	2564.48	25.80
F 1s	686.00	5.50	13857.98	38.76
P 2p	136.00	5.09	393.75	2.27
Si 2p	105.00	5.76	361.59	3.08
Li 1s	57.00	5.17	194.62	21.77

c

Name	Pos.	FWHM	Area	At%
O 1s	533.00	5.55	1946.38	10.13
C 1s	286.00	5.33	3645.56	53.26
F 1s	687.00	5.60	7467.38	30.33
Cu 2p	934.00	5.78	2431.05	1.86
P 2p	136.00	5.39	265.74	2.22
Si 2p	105.00	4.90	177.52	2.20

d

Name	Pos.	FWHM	Area	At%
O 1s	535.00	6.86	2240.39	6.12
C 1s	288.00	9.29	1270.67	9.74
F 1s	687.00	8.24	22670.27	48.33
P 2p	137.00	8.50	1396.67	6.13
Li 1s	56.00	8.08	348.05	29.68

Figure 6. XPS survey spectrum of anode electrode using E-cell a) Pristine electrode, b) Electrode at rest in half cell configuration c) Electrode after one charging cycle d) Electrode after 1 charging and discharging cycle.

spectrum. There is a marked difference between the Raman spectrum of the discharged electrode depending upon whether an initial charge step was performed or not. When the test cell (**Figure 7f**) was first subject to discharge (Figure 7c), small vibration peaks in the Raman spectrum between 500 and 1000 cm^{-1} were visible which can be associated with SEI layer formation. The strong peak at 1086 cm^{-1} is associated with the SEI compound Li_2CO_3 on the graphite surface, formed due to solvent decomposition and intercalation.[46] However minimal vibration peaks (besides those of graphite) are observed if the discharging is performed following the first charging of the test cell. (Figure 7e). Also, the similarity between the Raman spectrum of pristine and charged-first electrode with the electrode at rest (Figure 7a,b,d), indicate the physical diffusion of the lithium ions at the rest state without external voltage forces involved, which is also evident from XPS of the electrode at the rest state (refer to XPS Figure 6b). Further, when first charging and then discharging is done for the test cell, the Raman spectrum of the electrode is almost identical to the pristine state electrode indicating minimum lithium compounds formed during the first lithiation process of SEI formation and the prevention of solvent co-intercalation. (Figure 7e)

3.3.3. *Ex Situ UPS Studies*

Ex situ UPS studies shed further light on the surface changes that occurred during various stages of cycling of the test cell electrodes, through work function studies. These could be explained by examining the two different scenarios by which the discharge mechanism of the test half-cell proceeded, that is, i) rest mode to discharge, or ii) charge mode to discharge. The work function of the electrode that was charged prior to the first discharge and the electrode at rest has been calculated. Before the discharge was initiated, the work function of electrode charged first (4.42 eV) was lower than the work function of electrode at rest (4.82 eV), implying the Fermi level of the charged electrode was higher in energy as compared to the Fermi level of the electrode at rest, to begin with. As a result, the transfer of electrons from the Fermi level of the lithium anode to the Fermi level of the electrode that is charged first is made more facile as compared to the transfer of electrons from the lithium anode to the electrode at rest.

After the discharge is complete, the work functions of both these electrodes have been calculated again, namely, the discharged electrode (final state of electrode discharged from rest) and charge-discharge electrode (final state of electrode dis-

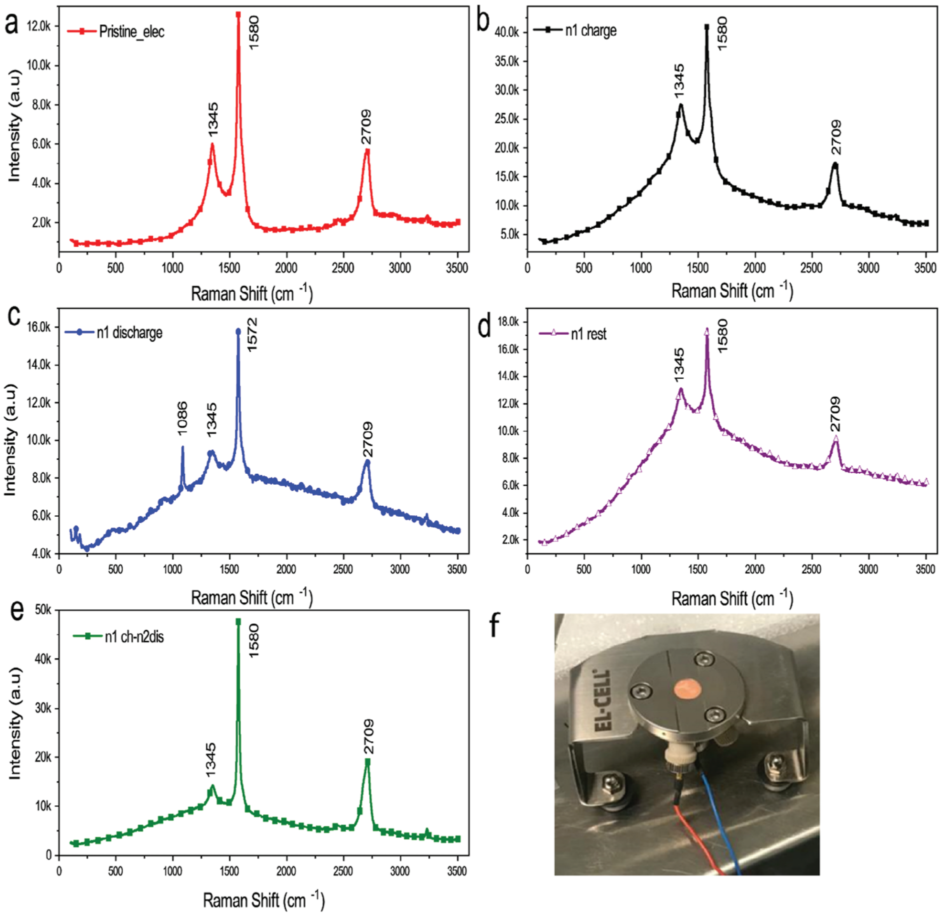

Figure 7. a) Raman spectrum of the pristine electrode. Ex situ Raman of the anode electrode b) After charging c) After discharging d) At rest after half cell formation without cycling e) Charge and discharge. f) EL-Cell used for in situ studies.

charged with a prior charge after the rest period. After discharge, the Fermi level of both cathodes in essence have been raised, as expected, but the one which was discharged after prior charging has its Fermi Level raised higher as compared to the one which was just discharged from the state of rest. The work functions of the final states of both these electrodes are 3.12 and 3.92 eV, respectively. The actual rise in Fermi levels in electron volts associated with both discharges is 1.3 eV [4.42 eV (beginning) – 3.12 eV (completion)] and 0.9 eV [4.82 eV (beginning) – 3.92 eV (completion)] respectively. Thus, the driving force for the transfer of electrons from the half-cell lithium anode to the electrode with a prior charge is higher. Consequently, more lithium ions can intercalate before the discharge cutoff of 0.01 V is reached, confirming an improvement in lithium- ion insertion capacity when the electrode is charged first before discharging. **Figure** 8e,f shows a schematic comparison of the relative Fermi levels alignments.

Another observation to take notice of is the work functions and UPS spectra of the pristine electrode and the electrode at rest overnight. Although there is no change in the value of the work function observed, the difference in shape of the UPS curves is conspicuous. In the literature, the change in curve shape with the addition of an extra peak is attributed to the decrease in the number oϕ π electrons with increase in σ electrons.[47] The loose ionic interactions between the positively charged lithium- ions from the electrolyte physically diffusing inside the GH electrode and the negative π bonded electron cloud above and below the graphene sheets of GH tend to reduce the number of π electrons, causing breakage of π bonds and formation of σ bonds, during the rest period.

Apparently, the positively charged Li ions were able to migrate toward the lithium reference anode under the influence of an applied negative potential on it, when the initial charge was performed, leaving behind the PF_6^{-1} ions. The XPS spectra of the electrode at rest in Figure 6b confirms the presence of phosphorus and fluorine, which assisted in subsequent lithiation of the GH electrode due to formation of an apparent *n*-type doped electrode. The extra Li^+ retrieved from the diffused state were able to add to the lithium inventory, free up lithiation sites, and hence increase the capacity of the electrode. The first charge after the rest period has also led to the absence of an early-stage lithium carbonate phase on the SEI, which was already at the nucleation stage on the electrode at rest. This contrast is evident by comparing the Raman spectrum of electrodes in Figure 7c,f and by observing the difference in the GCD curves of both half cells (Figure 5c,f) at 0.6 V that is associated with the formation of Li_2CO_3 on the SEI layer, due to the reaction between the lithium ions with the disintegrating solvent molecules after they co-intercalate with the simultaneous evolution of carbon dioxide.

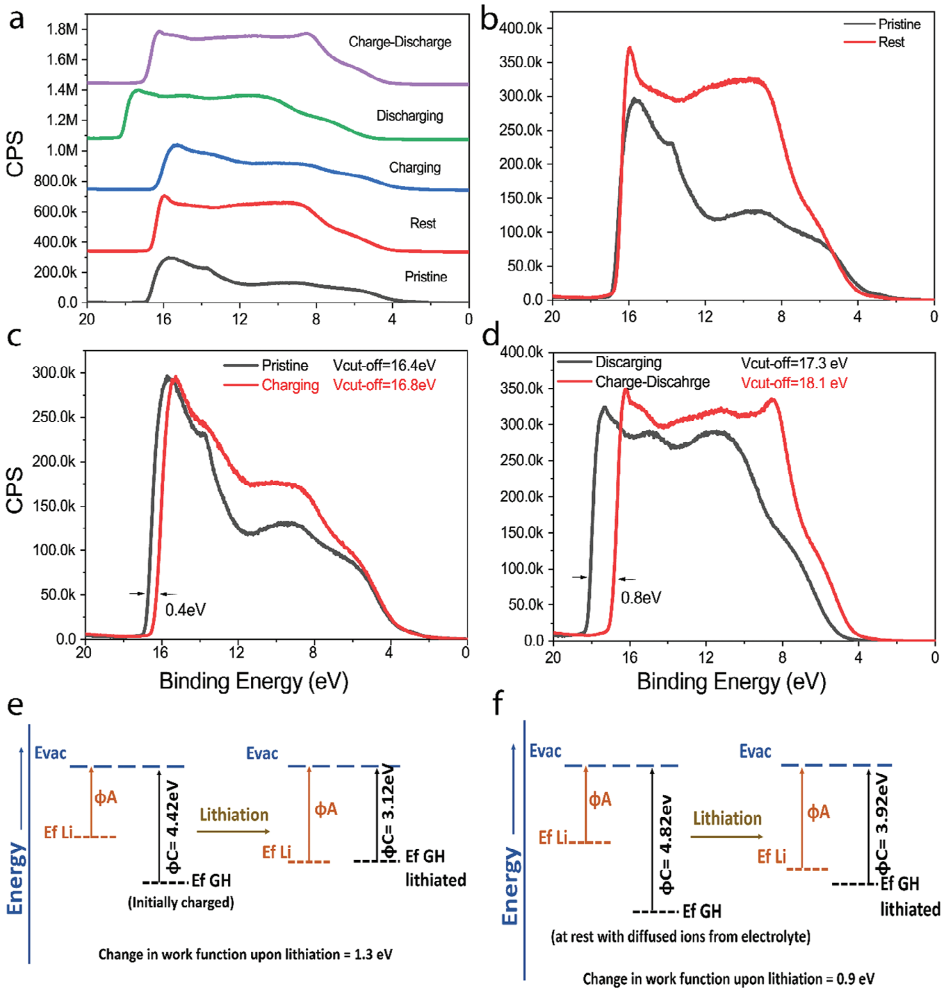

Figure 8. a) The UPS spectra of electrodes at different stages of cell cycling; comparison of spectral curves for b) pristine electrode and electrode at rest c) pristine electrode and electrode charged after period of rest before discharging d) electrode discharged from rest and electrode discharged after prior charge; schematic comparison of relative Fermi level alignments for two different discharge modes e) from prior charge mode to discharge f) from rest mode to discharge.

3.3.4. In Situ XRD Studies

In situ XRD patterns of GH graphite during charge and discharge are shown in **Figure 9**. The most obvious feature is the splits of graphite 002 and 004 peaks to LiC_{12} 002, 003 peaks and LiC_{12} 004, 005 peaks respectively (black arrows in Figure 9). These features are very similar to those observed from K^+ ion intercalation into graphite.[48] The diffraction peak shifts between graphite and LiC_{12} seems to be continuous, while those between LiC_{12} and LiC_6 are closer to a phase change jump.

Similar relationships between the 00*l* d-spacings of the Li^+ ion intercalated Li_xC_6 phases and the “n” number can be verified, in which the “n” number is defined to be the number of graphene layers between two intercalated Li^+ ion layers:

$$\begin{pmatrix} d_{00n} = \frac{d_i+d_0(n-1)}{n}; & d_{00(n+1)} = \frac{d_i+d_0(n-1)}{n+1} \\ d_{00(2n)} = \frac{d_i+d_0(n-1)}{2n}; & d_{00(2n+1)} = \frac{d_i+d_0(n-1)}{2n+1} \end{pmatrix} \tag{1}$$

where “d_i” stands for the Li^+ intercalated interlayer spacing, “d_0” stands for the empty interlayer spacing. It should be noted that the stoichiometric number “x” in Li_xC_6 equals 1/n. This explanation is successfully verified by modeling the above equations in DIFFRAC.TOPAS v7 to fit the measured in situ XRD patterns (**Figure 10**). The stoichiometric number “x” in Li_xC_6 can be directly refined from the measured peaks splits and plotted in Figure 9b.

4. Conclusion

Highly stable (GH) material was manufactured from waste strands of human hair with an in-house developed Joules Flash instrument. The material was investigated as an anode material in lithium-ion coin cells. In situ XRD analysis of the electrodes demonstrates the contraction and expansion of the layered, crystalline structure of GH during lithium intercalation and removal. Ex situ GH studies highlighted that the lithium-ion tends to diffuse into the graphite electrode during the rest stage after cell

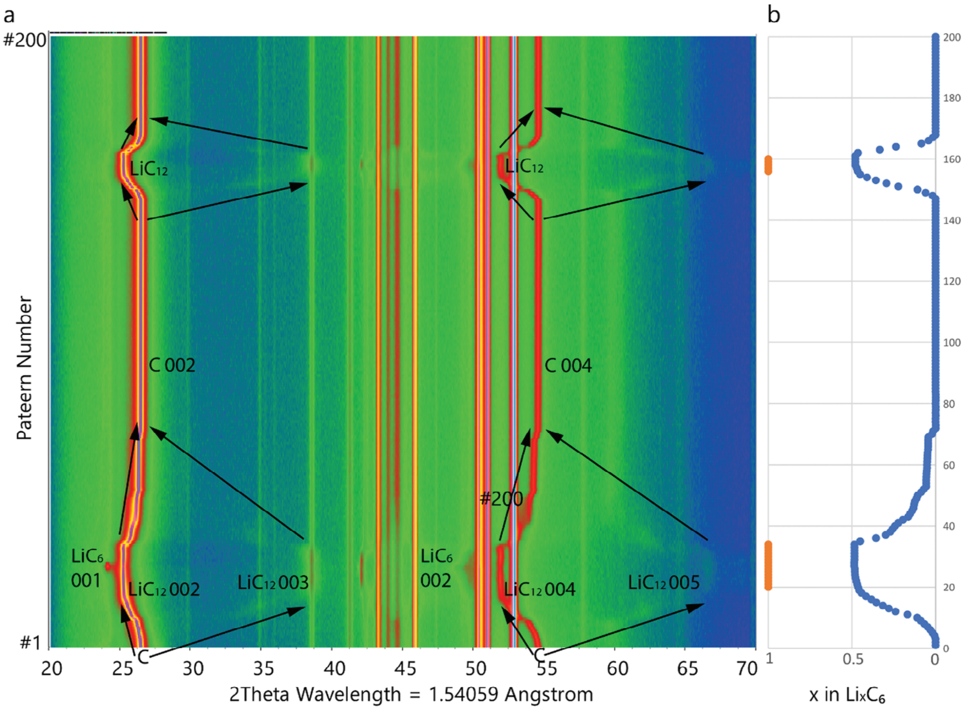

Figure 9. a) 2D plot of in situ XRD patterns of GH sample during charge and discharge. Graphite gradually changes to LiC_{12} phase then jump to LiC_6 phase, upon Li^+ ion intercalation; b) change of stoichiometric number "x" in Li_xC_6.

assembly and an initial first charge rather than discharge gives higher capacity as well as reduces unwanted lithium-ion reactions with other components such as from the solvent. This increases the life of the cell and at the same time its capacity. The increase in capacity by a simple variation in the SEI formation step is substantial, of ≈50% increase. These new insights will prompt further investigation into this phenomenon. This study will hopefully serve as a catalyst not only in the field of energy storage but in material science, to generate useful materials from what is generally considered to be waste. As shown above, such materials are waiting for their true value to be discovered, becoming next-generation raw materials. The investigators are further improving the reactor design and developing new materials for energy storage from waste.

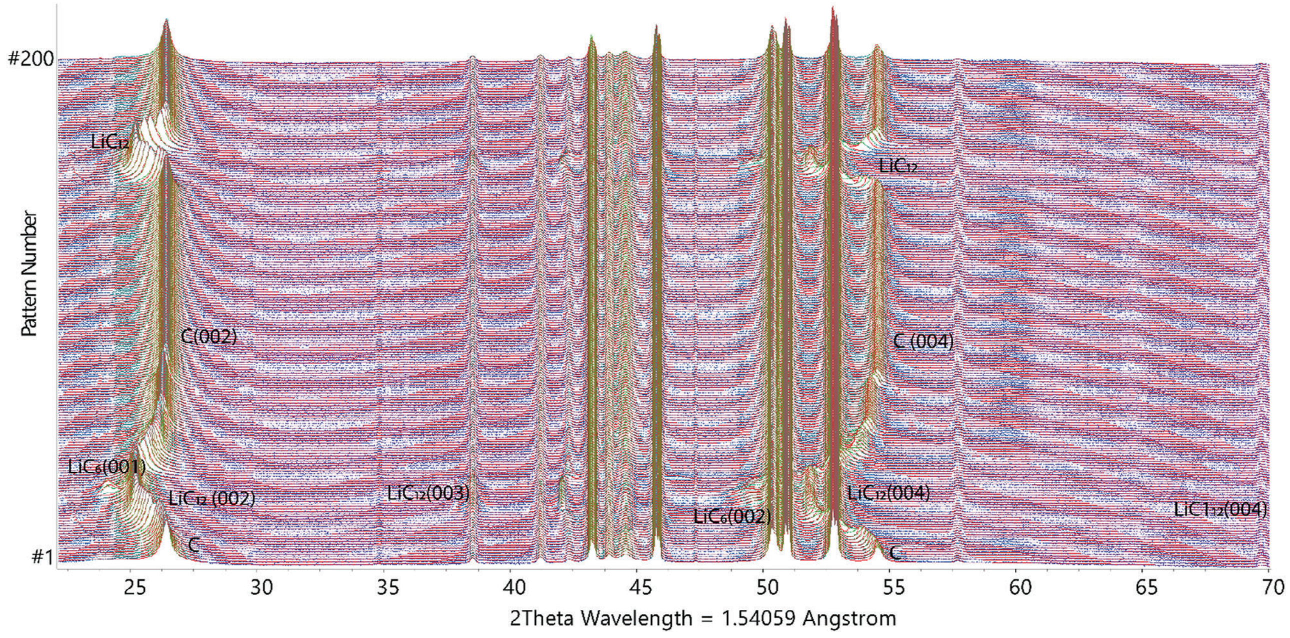

Figure 10. Simultaneous fittings of all in situ data using above equations.

Supporting Information

Supporting Information is available from the Wiley Online Library or from the author.

Acknowledgements

The authors are grateful for the financial support of J.K.'s scholarship provided by the Australian Research Council Training Centre for Future Energy Storage Technologies–StorEnergy (IC180100049), funded by the Australian Government and Calix Limited. The authors acknowledge the raw material and pre-processing support from Sustainable Salons. The authors acknowledge Dr. Joseph Fernando's support in setting the Gamry software measurements for in situ XRD. The authors acknowledge the project support from Queensland University of Technology; instrumentation and technical support of the QUT Central Analytical Research Facility (CARF) and the technical services of senior electrical technicians at QUT.

Open access publishing facilitated by Queensland University of Technology, as part of the Wiley - Queensland University of Technology agreement via the Council of Australian University Librarians.

Conflict of Interest

The authors declare no conflict of interest.

Data Availability Statement

The data that support the findings of this study are available in the supplementary material of this article.

Keywords

anode, battery, capacity, flash heating, graphite, hair, layer, surface, work function

Received: November 29, 2023
Revised: January 16, 2024
Published online: January 24, 2024

---

[1] L. Zhao, B. Ding, X. Y. Qin, Z. Wang, W. Lv, Y. B. He, Q. H. Yang, F. Kang, *Adv. Mater.* **2022**, *34*, 2106704.
[2] P. N. Martin Winter, J. O. Besenhard, M. E. Spahr, *Adv. Mater.* **1998**, *10*, 725.
[3] M. N. Obrovac, V. L. Chevrier, *Chem. Rev.* **2014**, *114*, 11444.
[4] D. Andre, H. Hain, P. Lamp, F. Maglia, B. Stiaszny, *J Mater. Chem. A Mater.* **2017**, *5*, 17174.
[5] J. Asenbauer, T. Eisenmann, M. Kuenzel, A. Kazzazi, Z. Chen, D. Bresser, *Sustainable Energy Fuels* **2020**, *4*, 5387.
[6] C. De Las Casas, W. Li, *J. Power Sources* **2012**, *208*, 74.
[7] N. Nitta, F. Wu, J. T. Lee, G. Yushin, *Mater. Today* **2015**, *18*, 252.
[8] N. A. Kaskhedikar, J. Maier, *Adv. Mater.* **2009**, *21*, 2664.
[9] M. Winter, B. Barnett, K. Xu, *Chem. Rev.* **2018**, *118*, 11433.
[10] S. Ragan, H. Marsh, *J. Mater. Sci.* **1983**, *18*, 3161.
[11] Ö. Kaya, M. Canbazoğlu, *Minerals Metallurg. Process.* **2009**, *26*, 158.
[12] X. Sun, Y. Chen, Y. Li, F. Luo, *Nanomaterials* **2023**, *13*, 82.
[13] P. Salimi, S. Tieuli, S. Taghavi, E. Venezia, S. Fugattini, S. Lauciello, M. Prato, S. Marras, T. Li, M. Signoretto, P. Costamagna, R. P. Zaccaria, *Green Chem.* **2022**, *24*, 4119.
[14] M. Curcio, S. Brutti, L. Caripoti, A. De Bonis, R. Teghil, *Nanomaterials* **2021**, *11*, 3183.
[15] A. M. Stephan, T. P. Kumar, R. Ramesh, S. Thomas, S. K. Jeong, K. S. Nahm, *Mater. Sci. Eng.: A* **2006**, *430*, 132.
[16] X. Zhou, F. Chen, T. Bai, B. Long, Q. Liao, Y. Ren, J. Yang, *Green Chem.* **2016**, *18*, 2078.
[17] N. Liu, K. Huo, M. T. McDowell, J. Zhao, Y. Cui, *Sci. Rep.* **2013**, *3*, 1.
[18] A. Su, J. Li, J. Dong, D. Yang, G. Chen, Y. Wei, *Small* **2020**, *16*, 1.
[19] A. Gupta, *J. Waste Managem.* **2014**, *2014*, 1.
[20] M. Brebu, I. Spiridon, *J. Anal. Appl. Pyrolysis* **2011**, *91*, 288.
[21] A. Singh, A. Wolff, S. D. Yambem, M. Esmaeili, J. D. Riches, M. Shahbazi, K. Feron, E. Eftekhari, K. Ostrikov, Q. Li, P. Sonar, *Adv. Mater.* **2020**, *32*, 1.
[22] A. S. Pannu, S. Sen, X. Wang, R. Jones, K. Ostrikov, S. Prashant, *Nanoscale* **2023**, *15*, 2659.
[23] N. D. Pham, A. Singh, W. Chen, M. T. Hoang, Y. Yang, X. Wang, A. Wolff, X. Wen, B. Jia, P. Sonar, H. Wang, *J. Mater. Chem. A Mater.* **2021**, *9*, 7508.
[24] A. Singh, E. Eftekhari, J. Scott, J. Kaur, S. Yambem, F. Leusch, R. Wellings, T. Gould, K. Ostrikov, P. Sonar, Q. Li, *Sustainable Mater. Technol.* **2020**, *25*, e00159.
[25] Q. Xie, Y. Zhang, D. Xie, P. Zhao, *J. Electroanalyt. Chem.* **2020**, *857*, 113749.
[26] S. Chen, P. Bao, L. Xiao, G. Wang, *Carbon* **2013**, *64*, 158.
[27] S. H. Bae, K. Karthikeyan, Y. S. Lee, I. K. Oh, *Carbon* **2013**, *64*, 527.
[28] C. Huan, X. Zhao, X. Xiao, Y. Lu, S. Qi, Y. Zhan, L. Zhang, G. Xu, *J. Alloys Compd.* **2019**, *776*, 568.
[29] X. B. Cheng, Q. Zhang, H. F. Wang, G. L. Tian, J. Q. Huang, H. J. Peng, M. Q. Zhao, F. Wei, *Catal. Today* **2015**, *249*, 244.
[30] A. M. A. Mohamed, S. Dong, M. Elhefnawey, G. Dong, Y. Gao, K. Zhu, D. Cao, *Chem. Phys. Lett.* **2023**, *815*, 140362.
[31] D. X. Luong, K. V. Bets, W. A. Algozeeb, M. G. Stanford, C. Kittrell, W. Chen, R. V. Salvatierra, M. Ren, E. A. McHugh, P. A. Advincula, Z. Wang, M. Bhatt, H. Guo, V. Mancevski, R. Shahsavari, B. I. Yakobson, J. M. Tour, *Nature* **2020**, *577*, 647.
[32] T. Oskabe, *Rigaku J.* **2017**, *33*, 15.
[33] M. Thommes, K. Kaneko, A. V. Neimark, J. P. Olivier, F. Rodriguez-Reinoso, J. Rouquerol, K. S. W. Sing, *Pure Appl. Chem.* **2015**, *87*, 1051.
[34] R. Bardestani, G. S. Patience, S. Kaliaguine, *Can. J. Chem. Eng.* **2019**, *97*, 2781.
[35] M. S. Dresselhaus, A. Jorio, R. Saito, *Annu. Rev. Condens. Matter Phys.* **2010**, *1*, 89.
[36] S. Reich, C. Thomsen, *Philos. Trans. R. Soc., A* **2004**, *362*, 2271.
[37] M. A. Pimenta, G. Dresselhaus, M. S. Dresselhaus, L. G. Cançado, A. Jorio, R. Saito, *Phys. Chem. Chem. Phys.* **2007**, *9*, 1276.
[38] G. E. Bacon, *Acta Crystallogr.* **1950**, *3*, 137.
[39] D. Hou, K. Li, R. Ma, Q. Liu, *J. Materiomics* **2020**, *6*, 628.
[40] A. K. Mishra, S. Ramaprabhu, *AIP Adv.* **2011**, *1*, 10.
[41] J. Xiao, Q. Li, Y. Bi, M. Cai, B. Dunn, T. Glossmann, J. Liu, T. Osaka, R. Sugiura, B. Wu, J. Yang, J. G. Zhang, M. S. Whittingham, *Nat. Energy* **2020**, *5*, 561.
[42] F. M. Courtel, S. Niketic, D. Duguay, Y. Abu-Lebdeh, I. J. Davidson, *J. Power Sources* **2011**, *196*, 2128.
[43] H. P. T. Sasanka Hewathilake, N. Karunarathne, A. Wijayasinghe, N. W. B. Balasooriya, A. K. Arof, *Ionics* **2017**, *23*, 1417.
[44] C. L. Fan, H. Chen, *J. Mater. Sci.* **2011**, *46*, 2140.
[45] B. Xing, C. Zhang, Y. Cao, G. Huang, Q. Liu, C. Zhang, Z. Chen, G. Yi, L. Chen, J. Yu, *Fuel Process. Technol.* **2018**, *172*, 162.
[46] S. Bhattacharya, A. T. Alpas, *Carbon* **2012**, *50*, 5359.
[47] H. Fukagawa, H. Yamane, T. Kataoka, S. Kera, M. Nakamura, K. Kudo, N. Ueno, *Phys. Rev. B: Condens. Matter Mater. Phys.* **2006**, *73*, 24.
[48] H. Onuma, K. Kubota, S. Muratsubaki, W. Ota, M. Shishkin, H. Sato, K. Yamashita, S. Yasuno, S. Komaba, *J. Mater. Chem. A* **2021**, *9*, 11187.